Supporting Information

Biggs et al. 10.1073/pnas.1308604110

SI Text

Absorption Spectra

The absorption spectra in the UV and X-ray regions are shown in Figs. S1 and S2, respectively.

Expressions for Stimulated X-Ray Raman Spectroscopy Signals

$$S_{\mathrm{I2P}}(\tau) = 2\Im\left\langle \alpha_2''(\tau)\alpha_1(0)\right\rangle = 2\Im\sum_{g'} e^{-i\omega_{g'g}\tau-\Gamma_{g'}\tau}\alpha''_{2;g\,g'}\alpha_{1;g'g}, \quad \text{[S1]}$$

where

$$\alpha_j = \alpha_j' + i\alpha_j'' = \sum_{e,g'g''} |g'\rangle\frac{\mu_{g'e}\mu_{eg''}}{2\pi}\int_{-\infty}^{\infty} d\omega\,\frac{\mathcal{E}_j^*(\omega)\mathcal{E}_j(\omega+\omega_{g'g''})}{\omega-\omega_{eg'}+i\Gamma_e}\langle g''| \quad \text{[S2]}$$

is the effective isotropic polarizability of the molecule, averaged over the spectral envelope of the jth ultrashort pulse, $\mathcal{E}_j$. $\omega_{g'g}$ and $\Gamma_{g'}$ are the excitation frequency and the phenomenological line width for the $g\to g'$ transition. In lieu of a more sophisticated model for interaction with the environment (bath), we set $\Gamma g' = 0.006$ eV for all valence-excited states for convenience. This is consistent with the electronic lifetime ($\Gamma_{g'}^{-1} = 100$ fs) typical for valence excitations. Core lifetime broadening coefficients were taken from ref. 1 and are $\Gamma_{\mathrm{Zn1s}} = 1.67$ eV, $\Gamma_{\mathrm{Zn2p}} = 0.70$ eV, $\Gamma_{\mathrm{Ni1s}} = 1.44$ eV, and $\Gamma_{\mathrm{Ni2p}} = 0.50$ eV.

The summation in Eq. **S1** is over the set of valence-excited states g'. This formula contains only the valence-excited coherence and ignores any core-excited population created by the first X-ray pulse. The core edges considered here, the K- and L-edges of zinc and nickel, have lifetimes of a few femtoseconds (1), after which Auger processes are expected to fill the core hole and ionize the molecule, taking it out of resonance with the probe pulse. Therefore, the signals presented here are accurate only for longer times. The stimulated X-ray Raman spectroscopy (SXRS) signal is experimentally collected in the time domain, and a numerical Fourier transform reveals the excitation frequencies of the valence-excited states that contribute:

$$S_{\mathrm{I2P}}(\Omega) = -\sum_{g'}\left(\frac{\alpha''_{2;gg'}\alpha_{1;g'g}}{\Omega_2-\omega_{g'g}+i\Gamma_{g'}} + \frac{(\alpha''_{2;gg'}\alpha_{1;g'g})^*}{\Omega_2+\omega_{g'g}+i\Gamma_{g'}}\right). \quad \text{[S3]}$$

The calculation of the effective polarizability requires the transition dipoles and energy differences between the set of valence states $|g'\rangle$ and the set of core-excited states $|e\rangle$. In Eq. **S2**, we see that those core-excited states whose excitation energies are within the pulse bandwidth will dominate the Raman process.

A 2D dispersed two-pulse (D2P)-SXRS signal is obtained by sending the probe through a spectrometer and recording the dispersed spectrum vs. the interpulse delay,

$$S_{\text{D2P-SXRS}}(t_2,\Omega_3) = \Im\mathcal{E}_2^*(\Omega_3)P^{(3)}(t_2,\Omega_3). \quad \text{[S4]}$$

A Fourier transform with respect to the delay time yields

$$S_{\text{D2P-SXRS}}(\Omega_2,\Omega_3) = \sum_{e,g'}\frac{iV_{ge}V_{eg'}(\alpha_{1;g'g})}{\Omega_2-\omega_{g'g}+i\Gamma_{g'}} \times\left(\frac{\mathcal{E}_2(\Omega_3+\omega_{gg'})\mathcal{E}_2^*(\Omega_3)}{\Omega_3-\omega_{eg}+i\Gamma_e} - \frac{\mathcal{E}_2^*(\Omega_3+\omega_{g'g})\mathcal{E}_2(\Omega_3)}{\Omega_3-\omega_{eg'}-i\Gamma_e}\right). \quad \text{[S5]}$$

SXRS Spectra

Figs. S3–S5 depict all 16 possible integrated two-pulse (I2P)-SXRS signals for the porphyrin dimer, in both the time and the frequency domains. The signals are labeled with the pulses listed from left to right, so that the Zn1s/Ni1s signal has the pump and probe tuned to the zinc and nickel K-edges, respectively. The signals have each been normalized before plotting.

There are four single-color I2P-SXRS signals shown in Fig. S4. In a single-color experiment, the doorway and window wavepackets are initially nearly identical. The Ni1s/Ni1s signal starts off large and decays exponentially. On top of this exponential decay is a high-frequency oscillation corresponding to the only significant peak in the Fourier transform spectrum, labeled herein as S_{98}, the 98th excited singlet state, at $\Omega = 6.13$ eV. A similar tale is told by the Zn1s/Zn1s signal. Here again there is a single dominant contribution, state S_{63} with a frequency of 5.48 eV.

The following two single-color I2P-SXRS signals use 2p orbitals for the core hole. The Ni2p/Ni2p spectrum features two strong peaks at $\Omega = 2.02$ eV and 2.58 eV, respectively (the first peak is actually two peaks, at 2.018 eV and 2.023 eV, which are unresolvable using the line width in this simulation). In the time domain this manifests as high-frequency oscillation, with a period matching the inverse frequency of the valence-excited states, on top of a lower-frequency oscillation corresponding to beat frequencies between the different Fourier components. The final single-color SXRS signal, Zn2p/Zn2p, in the main text is qualitatively different from the others.

The two-color I2P-SXRS signals come in two varieties: those that probe the same atom at different shells, such as the Ni2p/Ni1s signal, and those that probe different atoms, such as the Zn1s/Ni1s signal. The Ni1s/Ni2p signal shown in Fig. S5 has one dominant spectral component at $\Omega = 6.13$ eV, with smaller peaks at 4.03 eV and 7.08 eV. The time-domain signal is similar to the Ni1s/Ni1s signal; indeed, the dominant peak is in both spectra. The Ni2p/Ni1s signal in Fig. S6 is nearly identical to the Ni1s/Ni2p signal (they are taken with the same experimental setup, changing the delay time from positive to negative). Any difference between the two is related to the difference between α, which contains resonant and off-resonant contributions, and α'', which vanishes when the pulse is detuned off resonance. The corresponding zinc signals, Zn1s/Zn2p and Zn2p/Zn1s, have many different spectral components, and the overlap between doorway and window shows a complicated beating pattern.

It is the latter category of two-color I2P-SXRS signals, where the doorway and window wavepackets are created at different metal centers located on different porphyrin subunits, that most directly reports on excitation energy transfer (EET). The observable in an I2P-SXRS experiment is defined as the difference in probe transmission due to the presence of the pump and therefore would be zero if the monomers were uncoupled. The fact that the doorway and window wavepacket have nonzero overlap indicates that the valence systems of both monomers do indeed interact.

There are eight such signals, but given the near symmetry between signals taken with the pump and probe reversed, we can focus on only four: Ni1s/Zn1s, Ni1s/Zn2p, Ni2p/Zn1s, and Ni2p/Zn2p (all shown in Fig. S5). The Ni1s/Zn1s signal, which in the time domain starts at zero and grows in over the first 5 fs before decreasing again, is especially suggestive of back-and-forth excitation transfer between monomers. The roughly 10-fs period present in this signal matches the beat frequency between peaks at 6.56 eV and 6.13 eV, and the fact that the signal starts at zero is due to the fact that these peaks have opposite sign in the frequency domain.

Interestingly, the Zn2p/Ni1s and Zn1s/Ni2p signals are much more complex than the Zn1s/Ni1s and Zn2p/Ni2p signals. All four signals have in common that they start from zero and grow initially, but the Zn2p/Ni1s and Zn1s/Ni2p signals do not show strong coherent low-frequency motion.

Figs. S6–S9 show the D2P-SXRS signals, obtained by frequency dispersing the probe pulse. The one-dimensional I2P-SXRS signal is found by integrating the 2D D2P-SXRS signal. These signals show the coupling between core and valence excitations directly, allowing us to probe inside the effective polarizability. We see that the core states that dominate the X-ray absorption spectra (XANES) are not necessarily the most important for the SXRS signal. The former depend only on the dipole between the ground and the core states, whereas the latter depend also on the dipole between core and valence-excited states. Fig. S10 shows the largest-amplitude NTOs for the valence-excited eigenstates corresponding to the dominant peaks in Fig. 3 of the main text.

Natural Orbital Decomposition

Interaction with the pump creates the doorway

$$\left|\psi_D(\tau)\right\rangle = \sum_{g'} \alpha_{1;g'g_o} e^{-i\epsilon_{g'}\tau} \left|g'\right\rangle. \quad \text{[S6]}$$

This is a wavepacket of valence-excited states, each of which can be represented as a linear combination of particle–hole excitations

$$\left|g'\right\rangle = \sum_{ai} C_{ai}^{g'} c_a^\dagger c_i \left|g\right\rangle, \quad \text{[S7]}$$

where $c_a^\dagger$ (c_i) is the creation (annihilation) operator for the virtual (occupied) orbital a (i). We define the time-dependent transformation operator between the occupied and unoccupied orbital spaces,

$$\hat{K}(\tau) = \sum_{g,ai} \alpha_{1;g'g_o} C_{ai}^{g'} c_a^\dagger c_i e^{-i\epsilon_{g'}\tau}. \quad \text{[S8]}$$

The doorway can be obtained by acting with this operator on the ground state

$$\left|\psi_D(\tau)\right\rangle = \hat{K}(\tau)\left|g\right\rangle. \quad \text{[S9]}$$

The singular value decomposition (SVD) of $\hat{K}(\tau)$ provides a compact particle–hole representation of the doorway state in the space of single excitations (2),

$$K(\tau) = V(\tau) W(\tau) U^\dagger(\tau). \quad \text{[S10]}$$

The matrices $V(\tau)$ and $U(\tau)$ are unitary, and $W(\tau)$ is a diagonal matrix with real, nonnegative elements $w_\xi(\tau)$.

SVD allows to recast the doorway as

$$\left|\psi_D(\tau)\right\rangle = \sum_{\xi} w_\xi(\tau) c_\xi^\dagger(\tau) d_\xi(\tau) \left|g\right\rangle, \quad \text{[S11]}$$

where

$$c_\xi^\dagger(\tau) = \sum_a V_{a,\xi}(\tau) c_a^\dagger \quad \text{[S12]}$$

and

$$d_\xi(\tau) = \sum_i U_{i,\xi}^*(\tau) c_i \quad \text{[S13]}$$

are the creation and annihilation operators for the natural particle–hole orbitals, respectively. Because the doorway is normalized before application of the SVD, we have at all times

$$\sum_\xi w_\xi^2(\tau) = 1. \quad \text{[S14]}$$

The participation ratio, a useful measure of the degree to which the electron and the hole are entangled, is given by

$$R^{-1}(\tau) = \frac{1}{\sum_\xi w_\xi^4(\tau)}. \quad \text{[S15]}$$

In Fig. S11 we show the participation ratio for wavepackets at the K- and L-edges for zinc and nickel. We can see that Zn2p is unique in having a highly entangled electron and hole.

The Reduced Particle–Hole Densities

We define a density matrix corresponding to our pure state

$$\hat{\rho}(\tau) = \left|\psi(\tau)\right\rangle\left\langle\psi(\tau)\right|. \quad \text{[S16]}$$

This allows us to define the reduced particle density matrix

$$\begin{aligned} \sigma_p &= \mathrm{Tr}_h\left[\hat{\rho}(\tau)\right] \\ &= K(\tau)K^\dagger(\tau) \\ (\sigma_p)_{ba} &= \sum_\xi w_\xi^2 V_{\xi,a}^* V_{\xi,b}. \end{aligned} \quad \text{[S17]}$$

Similarly, we have for the hole

$$\begin{aligned} \sigma_h &= \mathrm{Tr}_e\left[\hat{\rho}(\tau)\right] \\ &= K^\dagger(\tau)K(\tau) \\ (\sigma_h)_{ij} &= \sum_\xi w_\xi^2 U_{\xi,i} U_{\xi,j}^*. \end{aligned} \quad \text{[S18]}$$

In real space we can write

$$\sigma_h(\mathbf{r}',\mathbf{r}) = \sum_{\xi,ij} \phi_j^*(\mathbf{r}') U_{\xi,j}^* w_\xi^2 U_{\xi,i} \phi_i(\mathbf{r}) \quad \text{[S19]}$$

and

$$\sigma_p(\mathbf{r}',\mathbf{r}) = \sum_{\xi,ab} \phi_b(\mathbf{r}') V_{\xi,b} w_\xi^2 V_{\xi,a}^* \phi_a^*(\mathbf{r}). \quad \text{[S20]}$$

The diagonal parts of these operators

$$\sigma_{h,p}(\mathbf{r}) = \int \sigma_{h,p}(\mathbf{r}',\mathbf{r}) \delta(\mathbf{r}-\mathbf{r}') \mathrm{d}\mathbf{r}' \quad \text{[S21]}$$

describe the spatial probability for finding the electron or the hole at a given point in space. Eq. **S21** is used to construct the density plots in Fig. 6 of the main text. The off-diagonal parts $\mathbf{r} \neq \mathbf{r}'$ represent spatial coherences.

1. Zschornack GH (2007) *Handbook of X-Ray Data* (Springer, Berlin Heidelberg), 1st Ed.

2. Martin RL (2003) Natural transition orbitals. *J Chem Phys* 118(11):4775–4777.

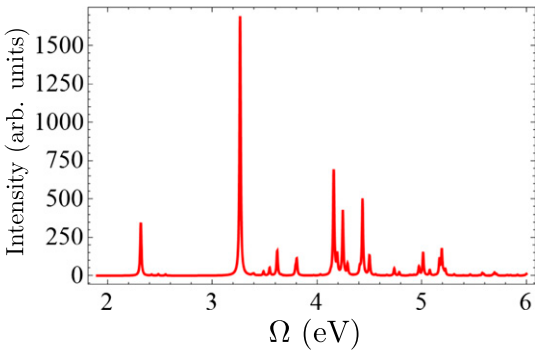

Fig. S1. UV absorption spectrum for the porphyrin dimer, using a uniform line width 0.006 eV.

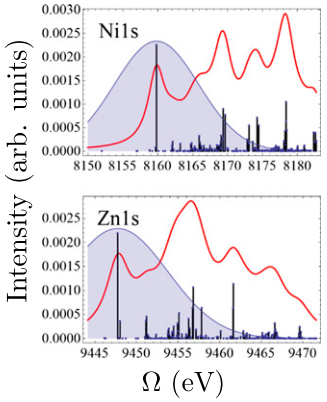

Fig. S2. Simulated K-edge XANES for zinc and nickel, using uniform line widths of 1.67 eV and 1.44 eV, respectively.

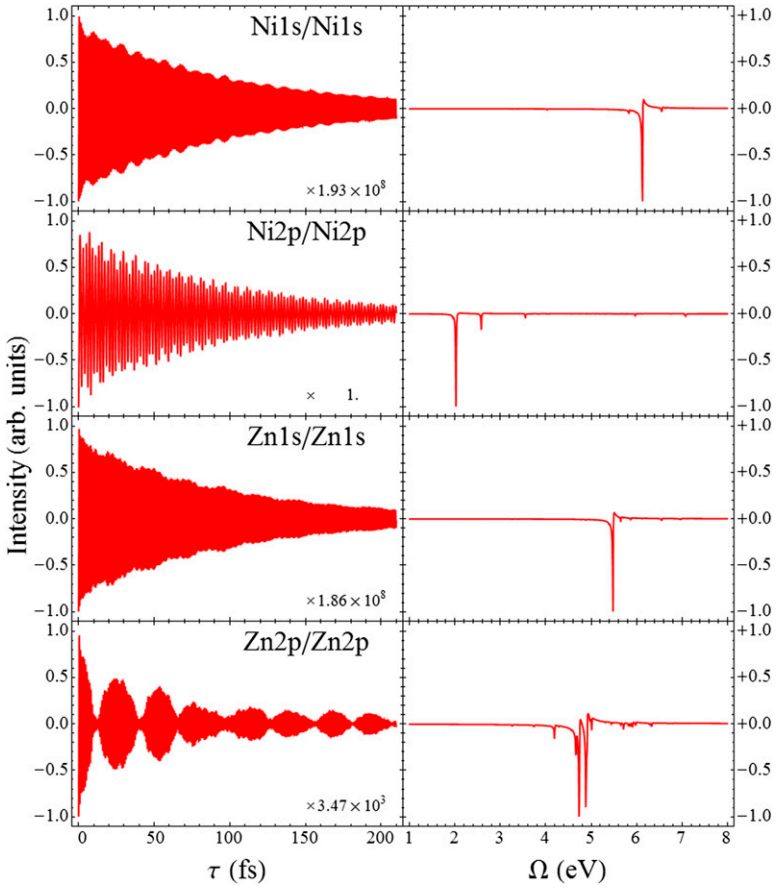

Fig. S3. Single-color I2P-SXRS signals from the porphyrin dimer.

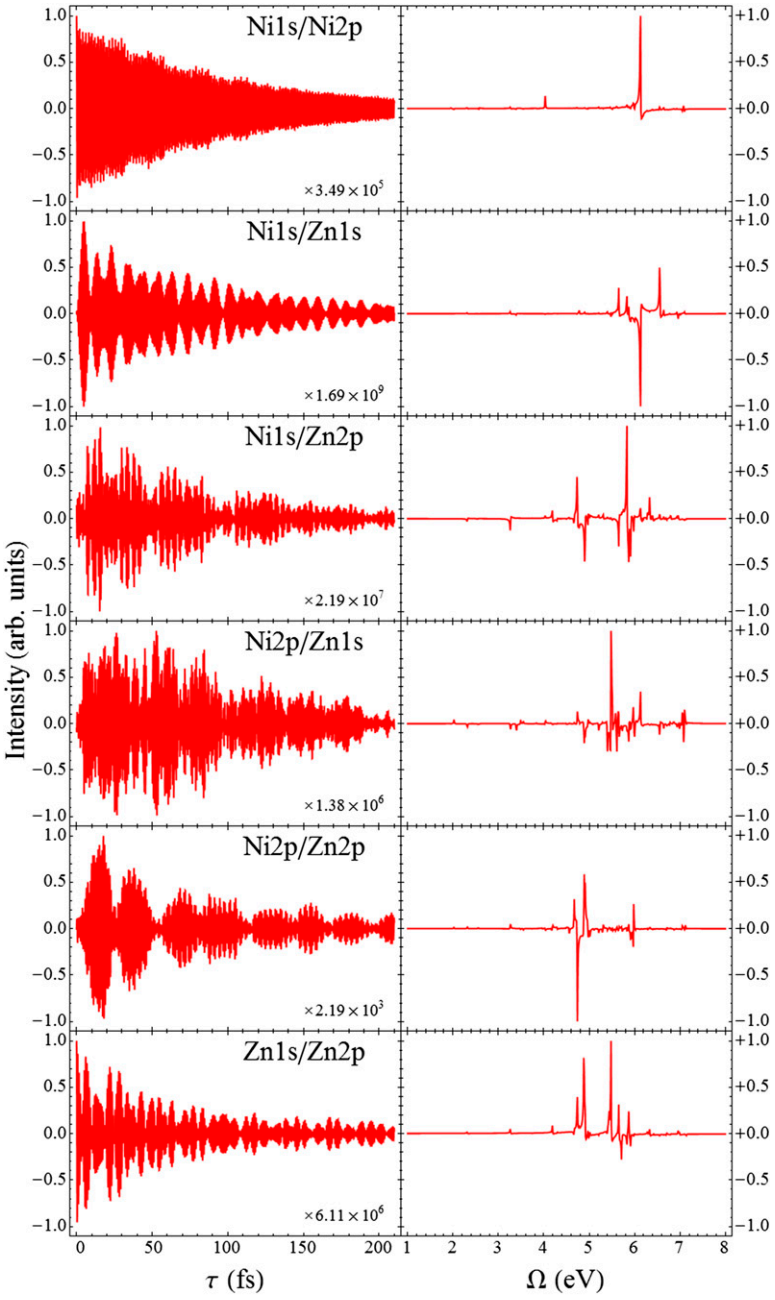

Fig. S4. Six of the two-color I2P-SXRS signals.

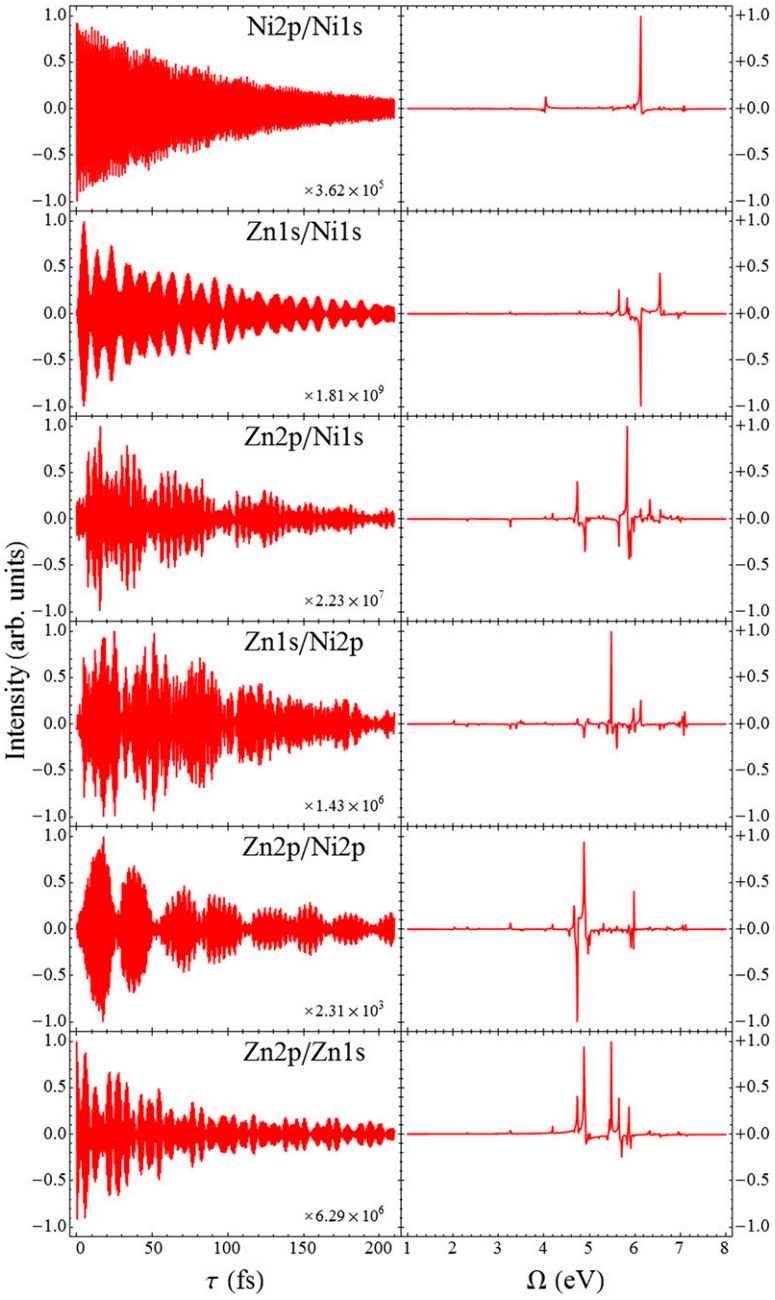

Fig. S5. The six two-color I2P-SXRS signals not shown in Fig. S4.

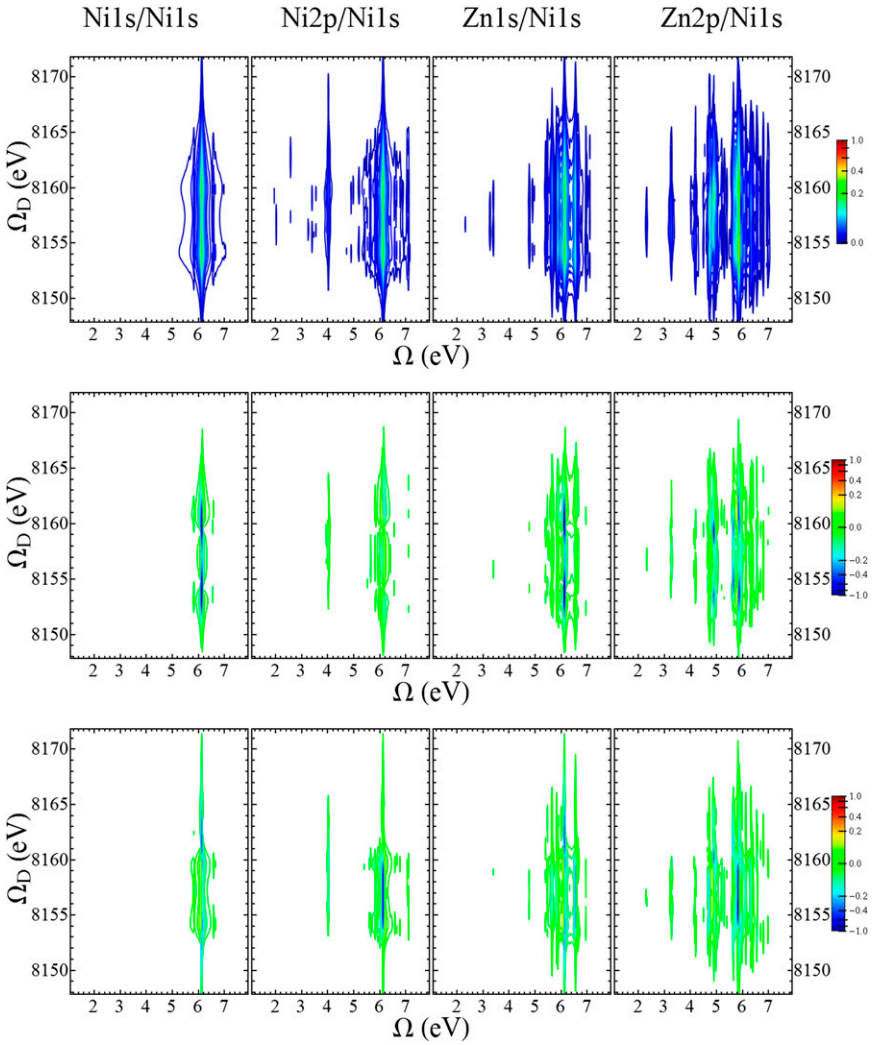

Fig. S6. Dispersed two-pulse Raman signal (Eq. **S5**), with the probe pulse at the nickel K-edge. The *x* axis is the Fourier conjugate of the delay time, and the *y* axis is the dispersed frequency. *Top*, *Middle*, and *Bottom* show the modulus, real, and imaginary parts of the signal, respectively.

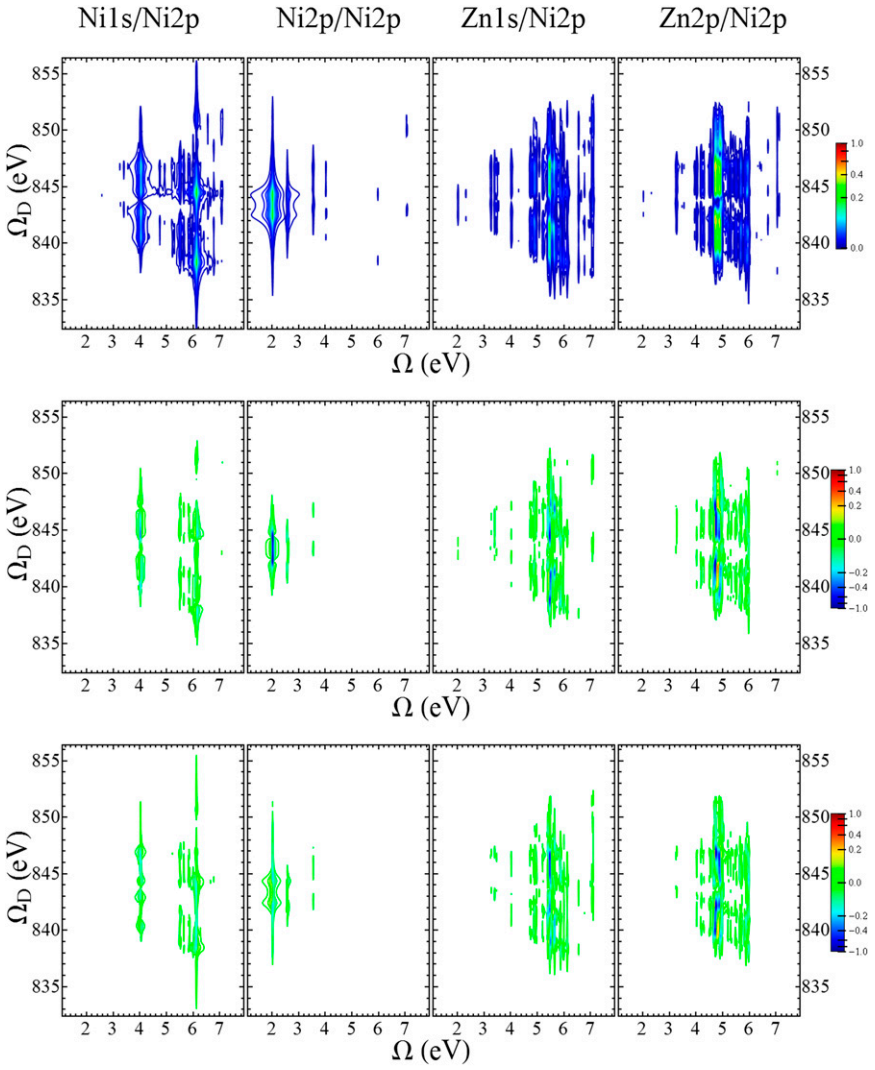

Fig. S7. The same as for Fig. S7 but with the probe tuned to the nickel L-edge.

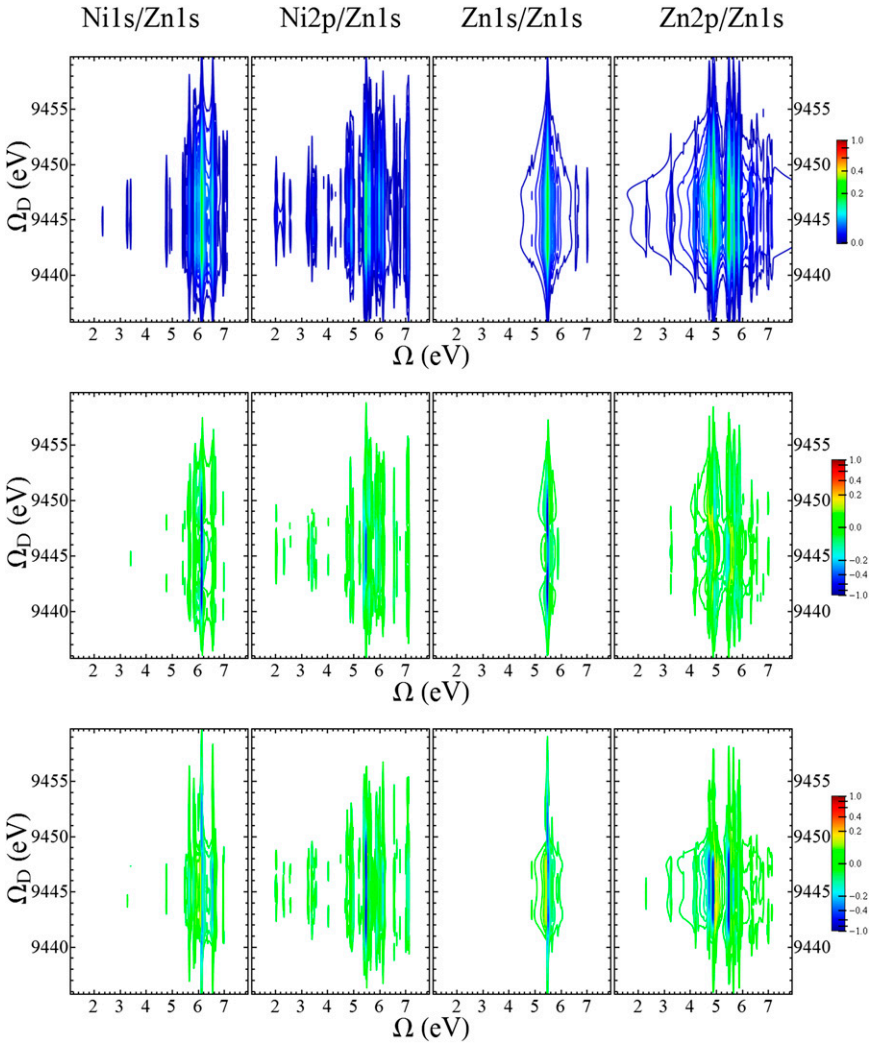

Fig. S8. The same as for Fig. S7 but with the probe tuned to the zinc K-edge.

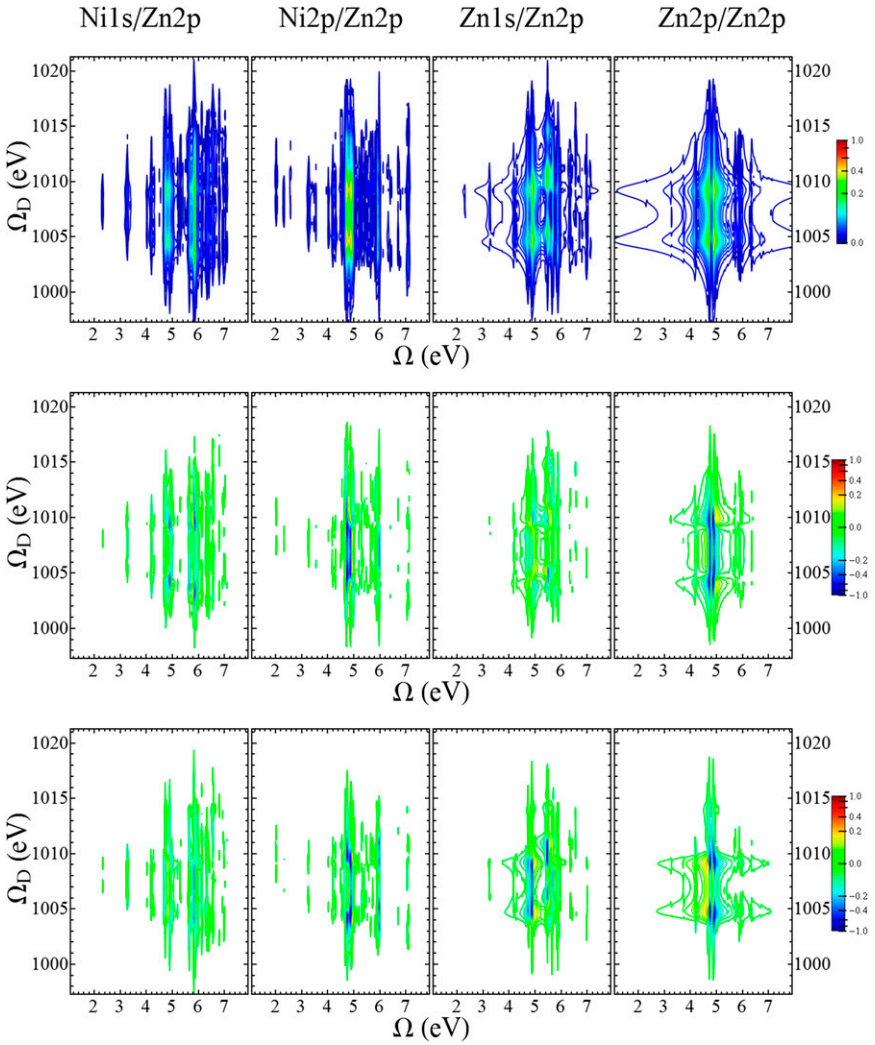

Fig. S9. The same as for Fig. S7 but with the probe tuned to the zinc L-edge.

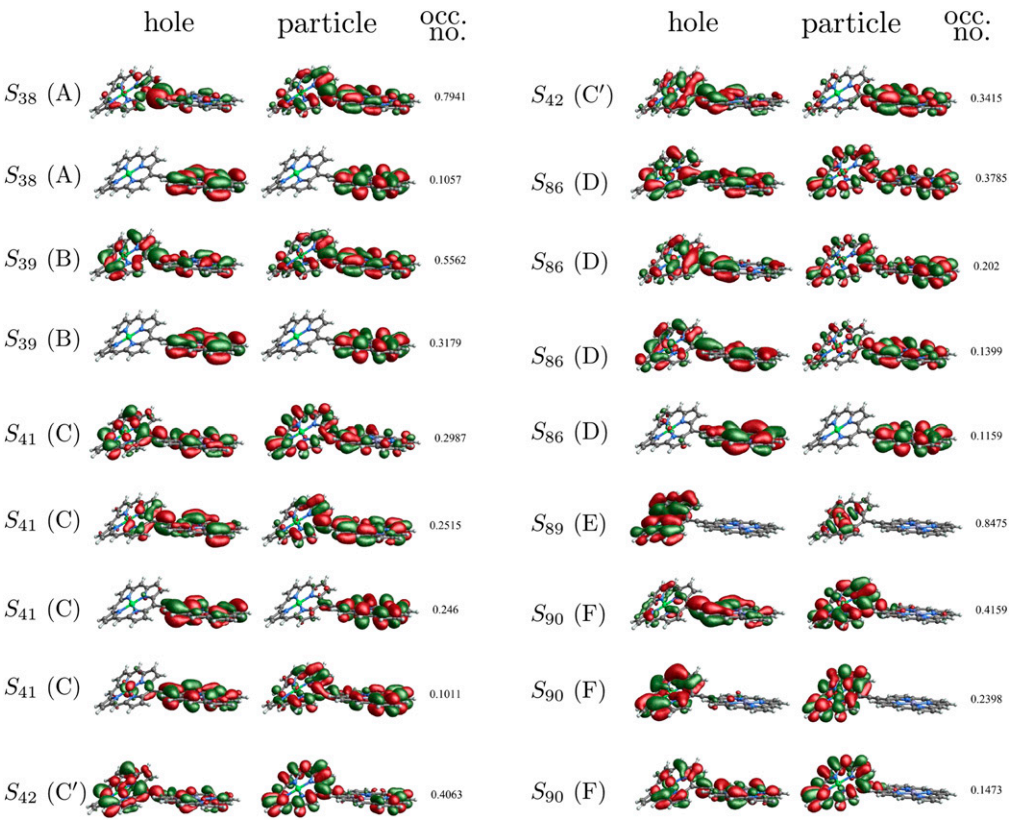

Fig. S10. Natural transition orbitals for the major peaks in the I2P-SXRS spectra shown in Fig. 3 of the main text. The occupation number is defined as w_ξ^2.

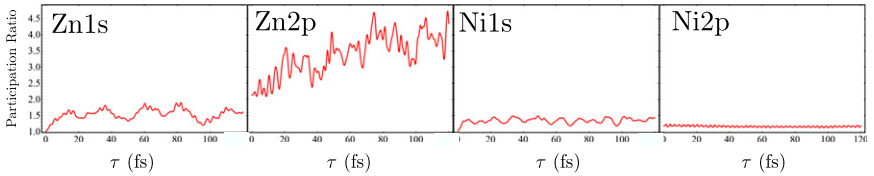

Fig. S11. Time-dependent participation ratios for valence wavepackets created by X-ray Raman excitation at the four core edges considered here, as indicated.

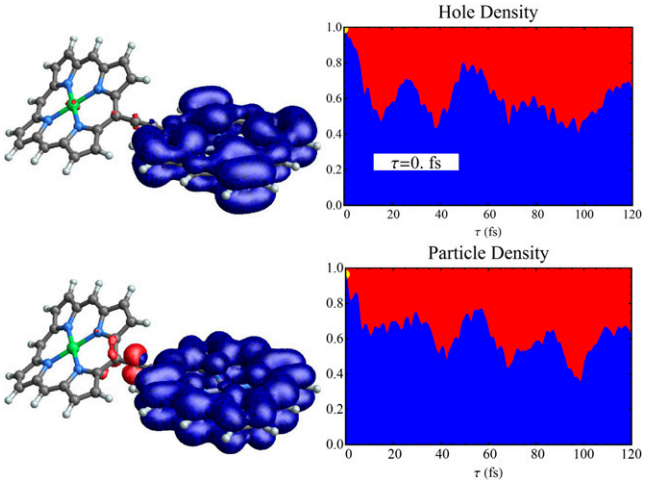

Movie S1. The electron and hole densities for the Zn2p doorway valence wavepacket for the first 120 fs following Raman excitation. (*Upper*) The reduced density for the hole. (*Lower*) The electron reduced density. (*Left*) Isosurfaces of the density, with red corresponding to the nickel monomer and blue to the zinc monomer. (*Right*) Plots of the integrated density, using the same color scheme. Initially, both electron and hole are entirely localized on the zinc monomer. Within 15 fs the hole is evenly delocalized between the monomers, following which there is coherent back and forth motion. The electron exhibits a similar trend, although the initial fast delocalization is not as complete.

Movie S1